Acta Materialia 226 (2022) 117612

Contents lists available at ScienceDirect

Acta Materialia

journal homepage: www.elsevier.com/locate/actamat

# Crack free metal printing using physics informed machine learning

B. Mondal, T. Mukherjee, T. DebRoy*

*Department of Materials Science and Engineering, The Pennsylvania State University, University Park, PA 16802, United States of America*

ARTICLE INFO

*Article history:*
Received 8 October 2021
Revised 29 December 2021
Accepted 29 December 2021
Available online 31 December 2021

*Keywords:*
Metal printing
Aluminum alloys
Powder bed fusion
Hot tearing
Heat transfer and fluid flow

ABSTRACT

Process parameters and thermophysical and mechanical properties of alloys affect cracking which remains a major challenge in metal printing. Cracks occur because of multiple mechanisms and currently, there is no unified mitigation strategy. Here we evaluate the effects of variables related to the physics of cracking computed by a mechanistic model and independent experimental data using machine learning to prevent cracking. The computed solidification stress, the ratio of the vulnerable and relaxation times, ratio of the temperature gradient to solidification growth rate, and cooling rates and experimental data are used to generate a cracking susceptibility index that predicts crack formation before printing. Computed values of these four variables when used in a decision tree, support vector machines, and logistic regression can predict crack formation with exceptional accuracy. Information gain, information gain ratio, and Gini index-based feature selection calculations provide the same comparative influence of these four variables. Results are presented as easy-to-use cracking susceptibility maps. Our approach can help in process optimization, designing new alloys, and solving problems in manufacturing beyond metal printing.



## 1. Introduction

Additive manufacturing (AM) can print unique metallic parts that cannot be fabricated by conventional manufacturing processes [1–3]. The powder bed fusion – Laser (PBF-L) process is a potentially attractive technique to make aluminum alloy parts in various industries due to their high strength-to-weight ratios [1–3]. Thin layers of alloy powders are melted by a laser beam and solidified layer upon layer to make complex parts with closely spaced features [2,4,5]. The repeated melting and solidification often generate cracks in parts [6], which significantly degrade their mechanical properties and serviceability [3,6].

The addition of inoculants [1] to form equiaxed grains and the application of external ultrasonic energy [7] to break up the long columnar grains have been tried to mitigate cracking. However, the type and amounts of inoculants and the intensity of the ultrasound energy are determined by trials. Cracking is also prevented by adjusting both the alloy composition and process variables such as heat source power, scanning speed, and preheat temperature [8–12]. The maximum slope of temperature versus square root of solid fraction has also been suggested as a cracking susceptibility criterion [13,14]. However, this criterion considers alloy composition and ignores process variables. Moreover, the effects of process variables often provide conflicting trends in cracking. For example, rapid scanning may enhance cracking by reducing the time for the liquid to reach the crack site [15]. However, slow scanning may result in larger pools that shrink more during solidification resulting in cracking [15]. Currently, there is no thorough understanding of the effects of process variables and properties of alloys on crack formation because they cannot be related to the mechanism of cracking.

The stress accumulated during solidification plays an important role in cracking [16]. The temperature gradients and solidification rates affect the solidification morphology and the scale of the microstructure both of which affect crack formation [3]. In the initial period of solidification, the low solid fraction allows the liquid to relax the partially solidified region. In contrast, in the final stage of solidification, the part becomes vulnerable to cracking because the high solid fraction obstructs the transport of the liquid to the crack site. The duration of both the vulnerable and the relaxation times are important for cracking [6]. The stress during solidification, the ratio of vulnerable and relaxation times, solidification morphology, and cooling rate are the mechanistic variables that are known to affect crack formation [3,6,16]. All these mechanistic variables are affected by both alloy composition and process parameters. In addition, the mechanisms of action of each of these mechanistic variables have been studied separately. However, what is needed but unavailable is an in-depth understanding of the collective roles of these mechanistic variables on crack formation. The values of each of these mechanistic variables can be calculated for each experimental condition and alloy composition using a mechanistic model.

* Corresponding author.
*E-mail address:* debroy@psu.edu (T. DebRoy).

https://doi.org/10.1016/j.actamat.2021.117612
1359-6454/

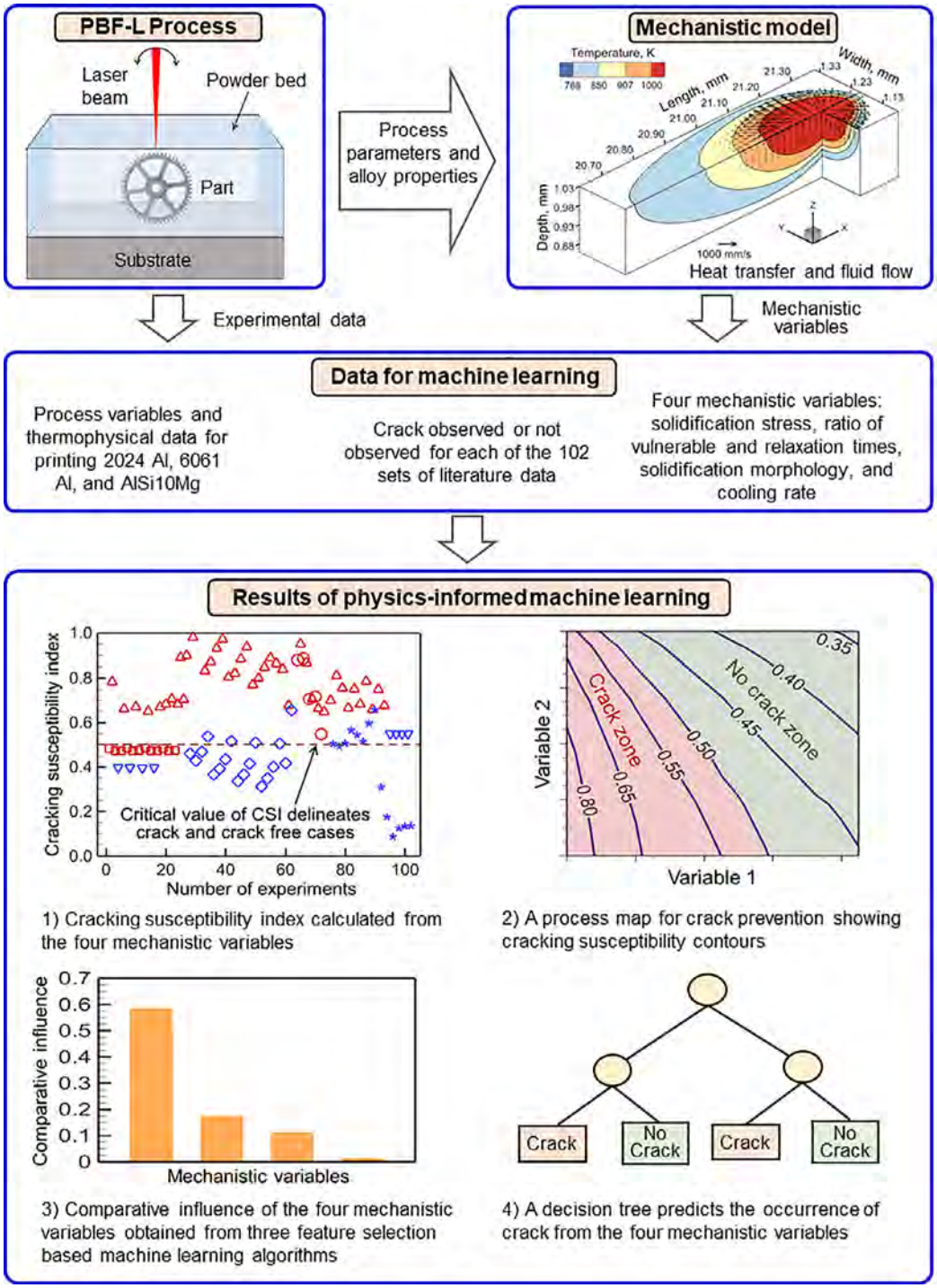


**Fig. 1. A Physics-informed machine learning towards crack-free printing.** Computed values of cooling rate and solidification morphology (indicated by the ratio of temperature gradient and solidification growth rate) at the trailing edge of the melt pool, the ratio of vulnerable and relaxation times, and solidification stress are used in a physics informed machine learning to accurately predict cracking during PBF-L of aluminum alloys. The combination of machine learning and mechanistic modeling gives a cracking susceptibility index, process maps for crack-free printing, the comparative influence of the important variables, and a decision tree to predict crack formation.

Here we show that cracks in printed metallic parts can be mitigated by physics-informed machine learning [17,18]. The physics of crack formation captured by the mechanistic variables is augmented into machine learning (ML) [19,20] to correlate with cracking occurrence for three aluminum alloys, 6061 Al, 2024 Al, and AlSi10Mg. Our approach involves mechanistic modeling [21], machine learning, and experimental data [9,10,22-26] and is schematically represented in Fig. 1. We develop and use a cracking susceptibility index to avoid cracking during PBF-L. Also, we determine the hierarchical order of mechanistic variables on crack formation.

## 2. Methodology

### 2.1. Physics-informed machine learning

Process variables along with thermophysical and mechanical properties of alloys affect crack formation. The twelve most important variables [1,6,12,27-29] include laser power, laser beam radius, scanning speed, layer thickness, preheat temperature, hatch spacing, specific heat, thermal conductivity, density, solidification range, maximum slope ($|dT/d(f_s)^{1/2}|$), and the Youngs modulus. To

quantitatively resolve the effects of these variables on cracking, at least $2^{12}$ (4096) experiments using the 2-factor design of experiments are needed [30]. The available experimental data do not satisfy this requirement for forecasting cracking based on the raw process variables and alloy properties. Currently, there is no available literature that evaluated the hierarchy of the above 12 variables and thermophysical properties.

As a solution, we use several mechanistic variables that represent the physics of crack formation. A similar analogy can be found in fluid mechanics where the dimensionless Reynolds number is used to represent the type of fluid flow (laminar or turbulent) through a cylindrical pipe instead of the variables viscosity, density, velocity, and pipe diameter. In the context of metal printing, several mechanistic variables that are based on physics and embody the role of multiple alloy properties and process variables can make the calculations tractable. The existing literature on cracking in fusion welding and AM points towards many such mechanistic variables, such as temperature gradient [3,6,8], solidification growth rate [3,6,8], cooling rate [3,6,8], solidification morphology [6,8], molten pool aspect ratio [3,6,27], mushy zone size [3,6], solidification stress [6,16,28], and the ratio of the vulnerable and relaxation times [6]. However, many of these variables are interdependent. Therefore, we have performed a statistical analysis using Pearson's correlation (see Appendix A1) to select variables that are independent and still represent the physics of cracking. These variables are the cooling rate during solidification [3,6,8], the ratio of the temperature gradient to the solidification growth rate [6,8], solidification stress [6,16,28], and the ratio of the vulnerable and relaxation times [6]. These four mechanistic variables need at least $2^4 = 16$ experimental data to accurately predict their role in crack formation. Here we show that a physics informed machine learning using the combined calculated mechanistic variables predict crack formation (Fig. 1) and highlight several unknown aspects of the problem.

Physics informed machine learning provides physics based correlation of crack formation with the mechanistic variables. For example, the computed values of solidification growth rate and temperature gradient, along with other variables can be correlated with the formation of crack using machine learning. Lower values of the temperature gradient to solidification growth rate ratio promote equiaxed grains and resist cracking. Both temperature gradient and solidification growth rate along with other mechanistic variables can be readily estimated using mechanistic models of PBF-L that solve the Navier Stokes and energy conservation equations using alloy properties and process parameters as inputs [21].

Physics informed machine learning using the four mechanistic variables helps lower cost, reduces experimental trials, and sheds light on the crack formation mechanism using the current knowledge base of metallurgy.

### 2.2. The calculation of mechanistic variables based on heat transfer and fluid flow model

The four variables which affect crack formation are cooling rate [31,32] during solidification ($\tau$), the ratio of the temperature gradient to the solidification growth rate [3,8] ($\varepsilon$), solidification stress [6,16] ($\sigma$), and the ratio [6] of vulnerable and relaxation times ($\beta$). Their mechanisms of action along with the process of calculation (Fig. 2) are discussed below.

#### 2.2.1. The cooling rate during solidification ($\tau$)

The cooling rates, indicated by the curved lines [3] in Fig. 2a, affect the grain size and cracking [31]. The ductility-based models relate critical strain rate to cracking. The rate of strain generated with the decrease in temperature is inversely related to the cooling rate and the ranking of various alloys by this metric agrees with welding [31]. Rapid cooling also refines the grains [32] which hinders crack propagation and reduces cracking [12]. The cooling rates during solidification are calculated between the liquidus and solidus isotherms at the trailing edge of the molten pool (Fig. 2c) on the top surface where cracks commonly form [33–35]. The cooling rates are calculated using a well-tested heat transfer and fluid flow model which is discussed in the Appendix A2. The properties of the three aluminum alloys utilized in the modeling are provided in Table 1.

#### 2.2.2. The ratio of temperature gradient to solidification growth rate ($\varepsilon$)

The slope of the straight lines in Fig. 2a, represents the value of $\varepsilon$ which affects morphologies [3] of the solidified alloys. Low ratios result in equiaxed grains often near the centerlines of the deposits [3], (Fig. 2a). Equiaxed grains reduce the susceptibility to crack formation [8]. Columnar grains form at high values of the ratio and make the microstructure susceptible to cracking (Fig. 2a). The calculation of $\varepsilon$ is also performed at the same location as the cooling rate using the heat transfer and fluid flow model (see Appendix A2).

#### 2.2.3. The ratio of the vulnerable and relaxation times ($\beta$)

Crack forms during the last stage of solidification [6] between solid fractions of 0.90 and 0.99. The part is vulnerable to cracking during this time, which needs to be viewed in comparison with the time during which liquid feeding of the solidification shrinkage can occur readily (Fig. 2d). It is now accepted [6,36,37] that sufficient liquid feeding is available between solid fractions of 0.4 to 0.9 which helps in strain relaxation. Furthermore, beyond a solid fraction of 0.99, the part is sufficiently strong to resist cracking [6,36,37]. The temperatures corresponding to these solid fractions can be estimated from the Scheil curves (see Appendix A3) for each alloy simulated using a commercial software (ThermoCalc). Since we have the transient temperature field from heat and fluid flow calculations (see Appendix A2), the times corresponding to solid fractions of 0.4, 0.9, and 0.99 can be readily obtained. Therefore, the vulnerable and relaxation times ratio was calculated from the computed temperature field and Scheil curve. The top surface temperature field was used for these calculations since the cracks originate at or near the melt pool trailing edge. The ratio of the vulnerable and relaxation times was calculated by considering the locations of the isotherms along the scanning direction. Solid fractions of 1 and 0 correspond to solidus and liquidus temperatures of an alloy, respectively. Similarly, the temperatures corresponding to solid fractions of 0.40, 0.90, and 0.99 were estimated [13,14] from the Scheil curve for each alloy (see Appendix A3). The time of solidification between 0.90 and 0.99 solid fractions was obtained by dividing the appropriate length corresponding to these solid fractions by the scanning speed. A similar procedure was followed for calculating the time for solidification between 0.40 and 0.90 solid fractions.

#### 2.2.4. Solidification stress ($\sigma$)

A crack may initiate from the last remaining liquid in the inter-dendritic region under high solidification stress (Fig. 2b) [12,16,38,39]. The amount of the last remaining liquid may be obtained from the Scheil plots of T vs $(f_s)^{1/2}$ for different aluminum alloys (see Appendix A3). The maximum slope of these plots occurs at different solid fractions between 0.90 and 0.99. A gentle slope near the end of solidification indicates low cracking susceptibility. The volume of the liquid remaining at the solid fraction corresponding to the maximum slope affects the solidification stress. The calculation of the stress [38] that causes cracking is discussed as follows.

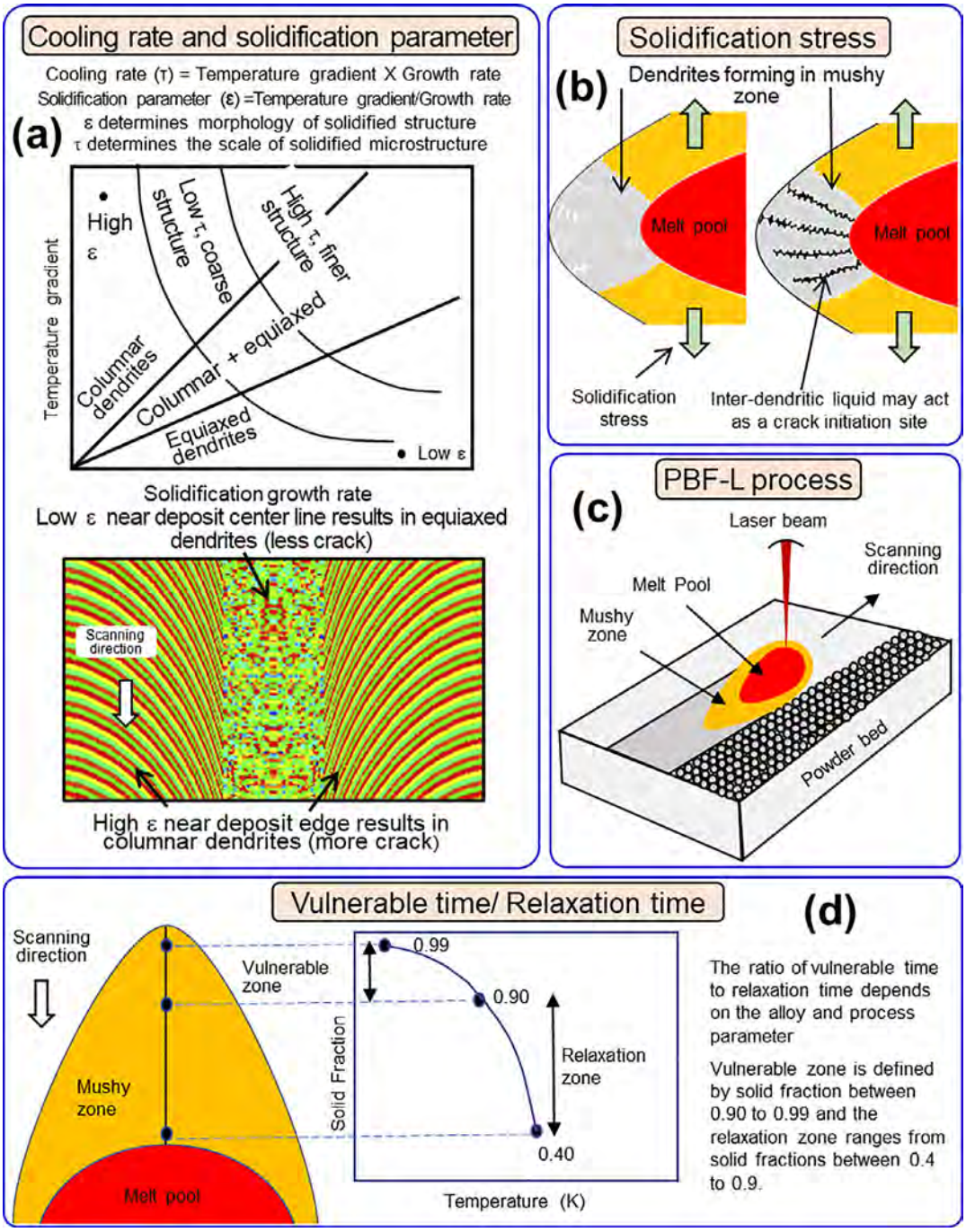


**Fig. 2. The role of mechanistic variables on crack formation.** **(a)** The cooling rate [33,34] affects the scale of the microstructure. The ratio of the temperature gradient to the solidification growth rate determines the morphology of the solidification microstructure [33,34] (adapted from 34). The formation of columnar and equiaxed dendrites at different locations of the deposit depends on the local solidification parameters (adapted from *4*). **(b)** High solidification stress [6,12,16,36] can initiate cracking in the inter-dendritic region during the last stage of solidification. **(c)** In the PBF-L process, a laser beam melts alloy powder particles to form a molten pool (red region) and the mushy zone shown by the yellow region. **(d)** Insufficient liquid feeding [6,12,28,29,35] in the inter-dendrite region in the last step of solidification fails to compensate for solidification shrinkage and causes cracking. The three points on the solid fraction versus temperature plot correspond to the specific solid fractions in the mushy zone needed for the calculation of vulnerable and relaxation times.

The solidification stress ($\sigma_c$) was obtained following an established methodology [*16*] that considers tensile stress as positive.

$$\sigma_c = \sqrt{\frac{2E\gamma_S}{\pi a}} \tag{1}$$

where $E$ is the modulus of elasticity and $\gamma_S$ is the specific surface energy. The values of $E$ are provided in Table 1 and $\gamma_S$ was taken [16] as 0.035 J/m$^2$. The variable '$a$' is half of the length of an internal crack. The length of the crack was estimated from the amount of the liquid available in the mushy zone during the last stages of solidification, i.e., for a solid fraction varying between 0.90 to 0.99 where the slope of the Scheil curve (T versus ($|dT/d(f_s)^{1/2}|$)) is maximum for the three aluminum alloys. Solid fractions of 0.93, 0.97, and 0.99 were used for 2024 Al, AlSi10Mg, and 6061 Al alloy, respectively (see Appendix A3). The volume of the remaining liquid was calculated by multiplying 0.07, 0.03, and 0.01 by the corresponding mushy zone volume for 2024 Al, AlSi10Mg, and 6061 Al alloys, respectively. The length scale of the crack was taken as the

**Table 1**
The temperature-dependent properties of three aluminum alloys utilized in the calculations. Here, 'T' represents temperature in K. The density is taken at room temperature, the latent heat of fusion at the liquidus temperature, and viscosity at liquidus temperature [3,4]. The temperature dependence of density and viscosity have been ignored in the calculations because the errors due to these simplifications are small.

| Properties | AA2024 | AA6061 | AlSi10Mg |
|---|---|---|---|
| Liquidus temperature (K) | 907 | 925 | 867 |
| Solidus Temperature (K) | 768 | 781 | 831 |
| Thermal conductivity (W/mK) | $25.2 + 3.98 \times 10^{-1}T + 7.36 \times 10^{-6}T^2 - 2.52 \times 10^{-7}T^3$ | $25.2 + 3.98 \times 10^{-1}T + 7.36 \times 10^{-6}T^2 - 2.52 \times 10^{-7}T^3$ | $113 + 1.06 \times 10^{-5}$ T |
| Specific heat (J/Kg K) | $930 - 6.27 \times 10^{-1}T + 1.48 \times 10^{-3}T^2 - 4.33 \times 10^{-8}T^3$ | $929 - 6.27 \times 10^{-1}T + 1.48 \times 10^{-3}T^2 - 4.33 \times 10^{-8}T^3$ | $536.2 + 0.035T$ |
| Density (Kg/m$^3$) | 2780 | 2700 | 2670 |
| Latent heat of fusion (J/Kg) | $297 \times 10^3$ | $335 \times 10^3$ | $425 \times 10^3$ |
| Viscosity (Kg/m s) | $1.3 \times 10^{-3}$ | $1.5 \times 10^{-3}$ | $1.3 \times 10^{-3}$ |
| $\frac{d\gamma}{dt}$ (N/m K) | $-0.35 \times 10^{-3}$ | $-0.40 \times 10^{-3}$ | $-0.35 \times 10^{-3}$ |
| Absorption coefficient in liquid | 0.3 | 0.3 | 0.3 |
| Absorption coefficient in powder | 0.7 | 0.7 | 0.7 |
| Modulus of elasticity (GPa) | 73 | 68.9 | 65 |

**Table 2**
Range of process variables and four mechanistic variables.

| Process variables | Range |
|---|---|
| Laser power (W) | 192 - 900 |
| Scanning speed (mm/s) | 75 - 2100 |
| Hatch spacing (mm) | 0.07 - 0.3 |
| Layer thickness (mm) | 0.03 - 0.1 |
| Laser beam radius (mm) | 0.04 - 0.1 |
| Preheat temperature (K) | 298 - 773 |
| **Mechanistic variables** | **Range** |
| Solidification Stress (MPa) | 4.56 – 10.04 |
| Ratio of vulnerable and relaxation times | 0.13 – 4.67 |
| Solidification parameter (Ks/mm$^2$) | 0.76 - 31.14 |
| Cooling rate (K/s) | 43,815 - 6396,480 |

cube root of the volume of the remaining liquid. The crack length was found to vary between 30 $\mu$m and 148 $\mu$m, which is consistent with the reported [6,16] values of cracks in aluminum alloys.

### 2.3. Data used in the analysis

Our machine learning (ML) analysis is based on 102 literature data sets wherein 62 cases had cracks and 40 cases were without experimentally detected cracks [9,10, 22-25]. Each data set consists of process variables that are paired with the presence or absence of cracks. The four mechanistic variables were computed for each of these 102 cases using the process variables and alloy thermophysical properties in a heat transfer and fluid flow model. Table 2 lists the range of the process variables and four mechanistic variables for all the experimental data sets. The process variables and mechanistic variables for all experimental cases are given in the supplementary document.

### 2.4. Machine learning (ML) algorithms

Crack formation in PBF-L parts is a classification problem for specimens with and without cracks. Therefore, to predict crack formation we used decision tree, logistic regression, and support vector machines [20] all of which are well-known classification algorithms. These algorithms and their implementation are discussed in the supplementary information section. The calculations of logistic regression and support vector machine were performed in WEKA [40] using 102 data with 10-fold cross-validations.

The ranking of four mechanistic variables on cracking is based on three indices, Gini index (GI), information gain (IG), and information gain ratio (IGR). These three indices are calculated using three commonly used ML algorithms ID 3, C4.5, and CART (classification and regression tree), respectively [20,40]. Threshold values of each variable are used by these algorithms to separate the two classes i.e., crack and no cracks. The ranking was calculated from computed values of four mechanistic variables of the 102 data sets and the experimentally observed crack occurrence. A variable with the maximum value of IG and IGR is the most important. In contrast, a variable with the maximum influence on cracking should have the least GI. The calculation of ranking using the mechanistic variables is demonstrated in the supplementary information.

To provide a qualitative tool to predict cracking a decision tree based on the ID3 algorithm [40] was generated. The tree is constructed using the IG value of the four mechanistic variables corresponding to 102 data. Using the highest IG, the variable stress was selected as the root node. Based on the threshold the data was split and in succeeding steps, similar IG calculations were done on other variables till a leaf node was achieved. Computed values of the four mechanistic variables for a new experiment are evaluated using the tree to predict whether the crack will form.

## 3. Results and discussion

The combined effects of alloy thermophysical properties and process variables affect [41–43] the four mechanistic variables representing the physics of crack formation. For example, the cooling rate during solidification has been reported to change with the scanning speed and laser power [3,4]. Similarly, the temperature gradient to solidification growth rate ratio is affected by the scanning speed [3,4]. Solidification stress has been reported to depend on speed [41] and power [42]. The three alloys have widely varying molten pool geometry and temperature fields which control the four mechanistic variables and hence susceptibility to crack formation (Fig. 3). Individually none of the four computed mechanistic variables can predict cracking susceptibility. However, these four variables can accurately predict crack formation when they are used in combination in machine learning.

### 3.1. Prediction of the crack formation using physics informed machine learning

Computed values of the four mechanistic variables are used in different ML algorithms to predict the occurrence of cracks in printed aluminum alloy parts. The prediction of crack formation is a classification problem with two classes of output, crack and no crack. The decision tree is a classification-based ML tool that can classify the input data based on the occurrence of crack formation. The decision tree (Fig. 4a) can predict the occurrence of cracks from the four calculated mechanistic variables. The construction of the decision tree is explained in Section 2.4. For any new sets of processing conditions, calculated values of the four mechanistic variables are classified using the tree to predict crack formation. The decision-making starts with the solidification stress and continues by checking the values of other mechanistic variables until a decision is made on the crack formation. The decision tree

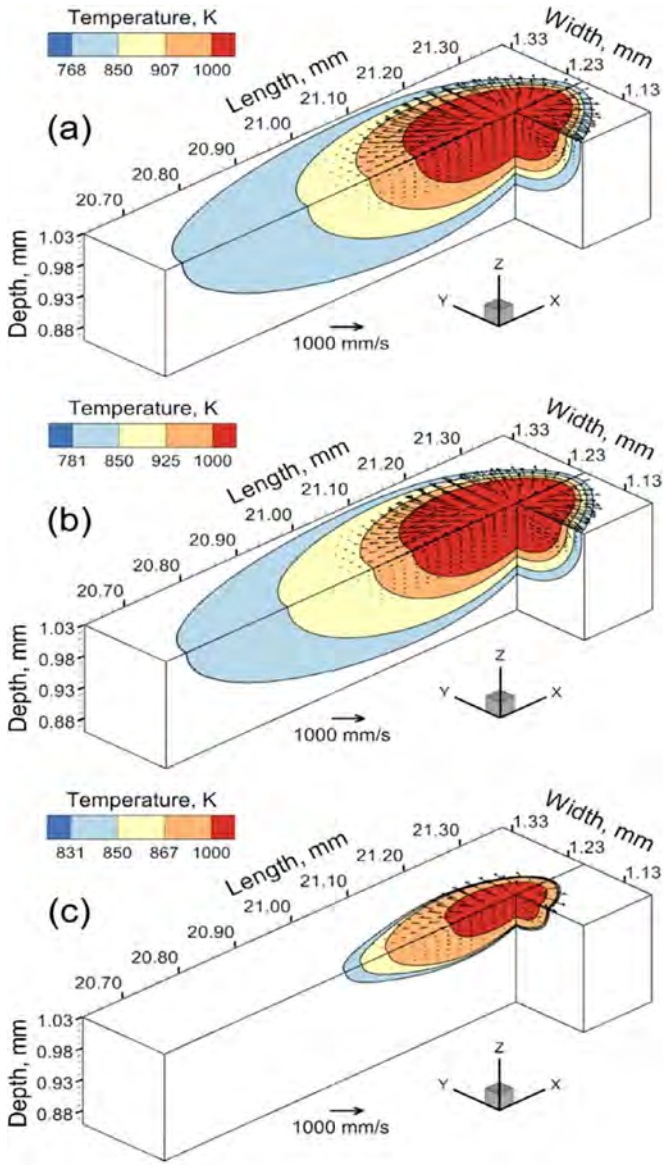


**Fig. 3. Calculated temperature and velocity distributions in 3D.** The alloy properties and process variables significantly affect the three-dimensional temperature and velocity distributions that are used to compute the four mechanistic variables. The velocity fields, dominated by Marangoni convection [3], affect the temperature fields and melt pool geometry. The process variables such as the laser power (500 W), scanning speed (2000 mm/s), layer thickness (30 $\mu$m), and beam radius (50 $\mu$m) were kept constant for the printing of **(a)** 2024 Al, **(b)** 6061 Al and **(c)** AlSi10Mg. Temperature contours are shown in the legend of each figure. Vectors representing the velocity of fluid flow are indicated by black arrows. Their magnitudes can be calculated by comparing their lengths with the reference vector. X, Y, and Z axes represent the scanning direction (positive X direction), the width, and the depth, respectively.

is proved to be accurate in predicting crack formation as evident from the corresponding confusion matrix (Fig. 4d). The construction of a confusion matrix and the method of computing accuracy from that are explained in the supplementary document.

Although the decision tree provides a visual tool to predict cracks, no quantitative correlation between the four mechanistic variables and crack formation can be obtained. Such quantitative relations can guide us to tune in the important variables to control cracking. Support vector machines can provide an algebraic equation of a hyperplane that separates the specimens with or without cracks (see the supplementary document). The equation of the hyperplane contains the four mechanistic variables. For a new set of experiments, the calculated values of the four mechanistic variables can be used in the equation to predict the formation of crack. Although support vector machines can predict crack formation accurately (see confusion matrix in Fig. 4e) the wide variety of data on crack formation corresponding to different values of four mechanistic variables makes the equation of the hyperplane cumbersome, as explained in the supplementary document. In addition, the presence of four input variables precludes a visual representation of the hyperplane.

The predictive performance of a regression-based model can be very good especially for a small dataset examined here. For a dataset with binary classes of output, logistic regression is often a good choice. It provides an algebraic equation to correlate the four mechanistic variables with the probability of occurrence of cracking (see supplementary document for details). The 'S'-shaped sigmoid function fitting (Fig. 4b) of experimental data using a logistic regression can predict the crack formation (Fig. 4f). However, the 70% accuracy of prediction is the lowest of the four classification algorithms and the use of non-linear, probability-dependent equation is not straightforward as explained in the supplementary document.

As an alternative to the low accuracy of the logistic regression for the dataset used, we explored linear regression (Fig. 4b). A prerequisite for fitting a linear equation with four input variables is that there must not be any interdependence among these variables. The Pearson matrix (Fig. 4c) provides the correlation coefficients among the four variables. The absolute values of the correlation coefficients less than 0.5 indicate no interdependence of the variables [44,45]. Therefore, the four mechanistic variables are linearly fitted to provide an algebraic equation that can predict crack formation with high accuracy (see the confusion matrix in Fig. 4g). Although the other algorithms are beneficial in the accurate prediction of cracking, the linear regression can provide a simple cracking susceptibility index which can provide many insights about crack formation as discussed below.

### 3.2. Cracking susceptibility index

A cracking susceptibility index (CSI) is an indicator that can predict the occurrence of cracks in printed parts using the four mechanistic variables that depend on process variables and alloy properties. The CSI is derived by relating the cracking frequency with the four mechanistic variables of 102 data sets (see the supplementary document) of literature data [9-10,22-25] for three aluminum alloys using linear regression. The crack occurrence is either 1 or 0 depending on whether cracks were observed or not.

The results obtained from the linear regression are used to derive an easy-to-use, verifiable cracking susceptibility index (CSI) as:

$$\mathrm{CSI} = 0.182\sigma + 0.135\beta + 0.014\varepsilon - 1.1 \times 10^{-8}\tau - 0.85 \qquad (2)$$

where the variables $\sigma$, $\beta$, $\varepsilon$, and $\tau$ indicate the computed values of solidification stress (in MPa), the ratio of vulnerable and relaxation times, the temperature gradient to the solidification growth rate ratio (in K-s/mm$^2$), and cooling rate (in K/s), respectively. Eq. (2) is applicable for the ranges of four mechanistic variables provided in Table 2. A high value of CSI correlates with higher cracking susceptibility. The calculated CSI values for the 102 data sets show that the CSI has a threshold value of 0.5 (Fig. 5). This threshold value could accurately predict all but 16 of the 102 experiments considered. The CSI for the alloy system examined has an accuracy of 84.3% as explained from the confusion matrix. This threshold value of 0.5 is valid for the three aluminum alloys studied here for the range of process conditions reported in Table 2. Threshold values higher than 0.65 and lower than 0.45 all correctly conform to the predictions of CSI. While all values greater than 0.65 corre-

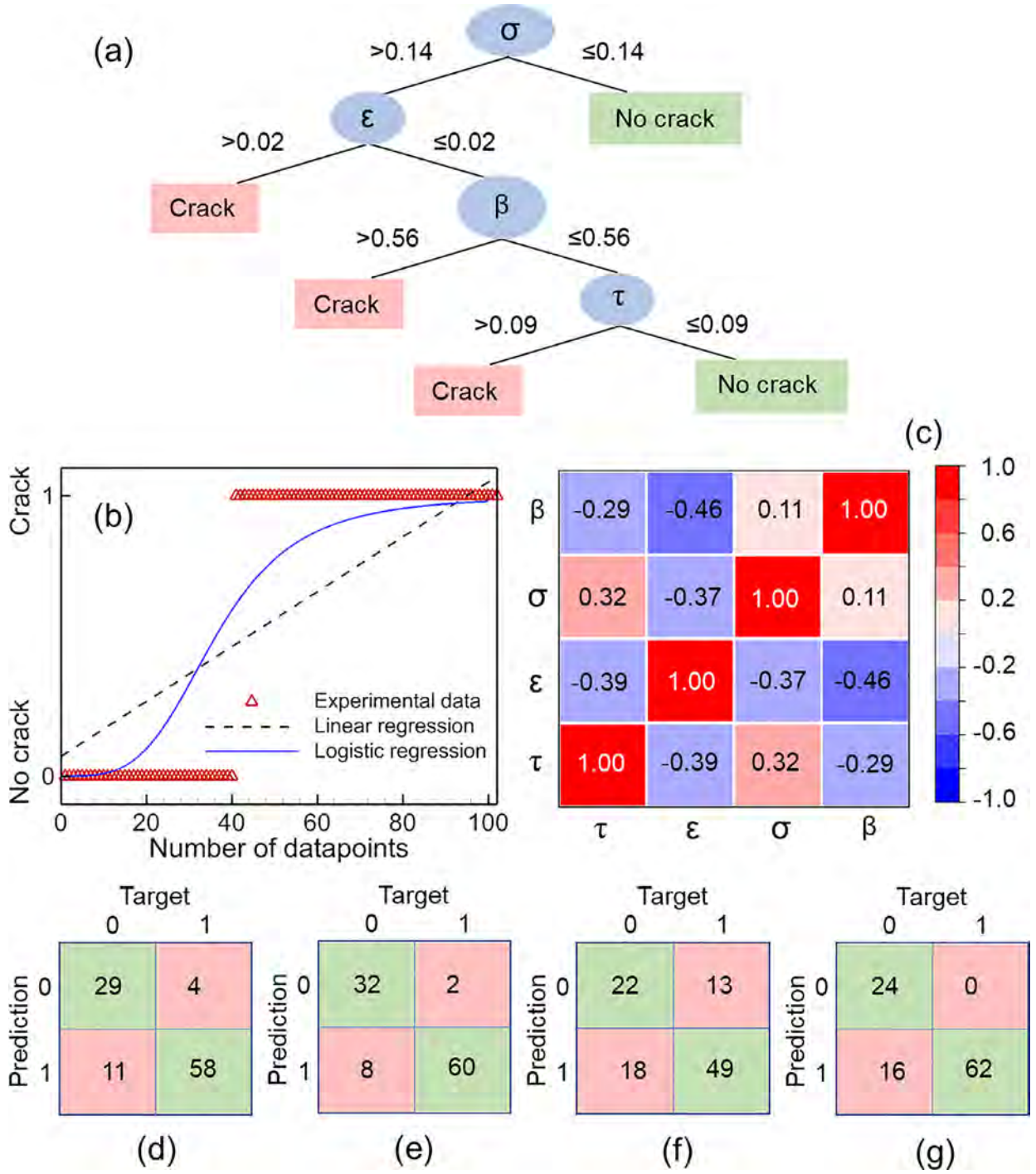


**Fig. 4. Applications of different ML algorithms to predict crack formation.** **(a)** A decision tree constructed using four mechanistic variables, $\sigma$, $\varepsilon$, $\beta$, and $\tau$ to predict crack formation in aluminum alloy printed parts. The decision-making criteria are based on the normalized values of the four variables. The methods of normalization and the construction of the tree are explained in the supplementary document. **(b)** An overlay of results of logistic regression and linear regression along with the experimental observation of crack formation. Here, 1 and 0 indicate specimens with or without cracks, respectively. The p-value for the linear regression was of the order of $10^{-5}$ **(c)** A Pearson matrix indicating the correlation coefficients among the 4 mechanistic variables. Absolute values of correlation coefficients less than 0.5 indicate less interdependence of the variables which is a prerequisite of fitting the variables using linear regression. Confusion matrices to evaluate the crack prediction ability of **(d)** decision tree, **(e)** support vector machines, **(f)** logistic regression, and **(g)** linear regression based on occurences of cracks. The construction of these confusion matrices and the method for predicting the accuracy of crack prediction from these matrices are described in the supplementary document. The computed accuracies of the decision tree, support vector machines, logistic regression, and linear regression are 85.3%, 90.2%, 70%, and 84.3%, respectively.

spond to the presence of cracks and values smaller than 0.45 correspond to crack-free cases, the intermediate values indicate specimens with or without cracks. The origin of this deviation from 0.5 is unknown. In addition, the sign before the coefficients in Eq. (2) indicates the type of relationship between the mechanistic variable and cracking. For example, $\sigma$, $\beta$, $\varepsilon$ with positive coefficients have a direct influence on cracking susceptibility which increases for higher values of these variables. Similarly, the negative coefficient of cooling rate, $\tau$, indicates diminished cracking susceptibility at higher cooling rates.

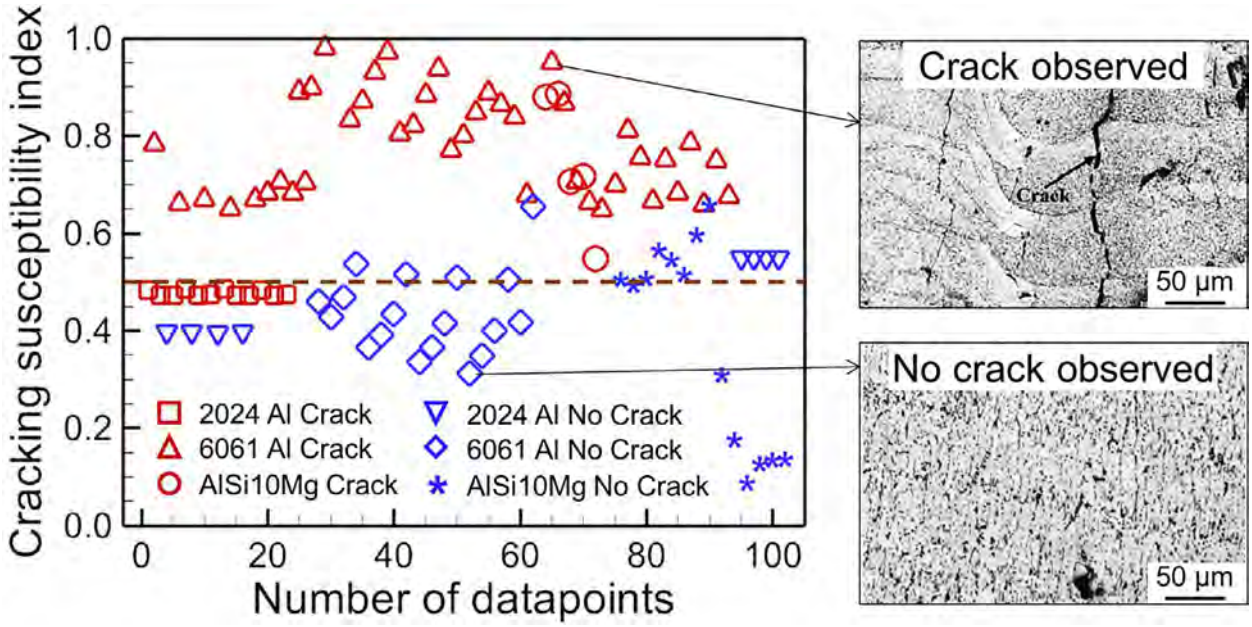


**Fig. 5. The effectiveness of the cracking susceptibility index (CSI).** The cracking susceptibility index obtained from the calculated values of four mechanistic variables can predict cracking. A threshold value of the index of 0.50 delineates the presence or absence of cracks. The required values of the four mechanistic variables needed for the estimation of the cracking susceptibility index can be obtained from a mechanistic model. The CSI is valid within the range of variables provided in Table 2. The values of the index for the 102-independent experimental data [9-10,22-25] are shown in the figure using different symbols. The two micrographs for PBF-L of 6061 Al alloy [9] are consistent with the cracking susceptibility index.

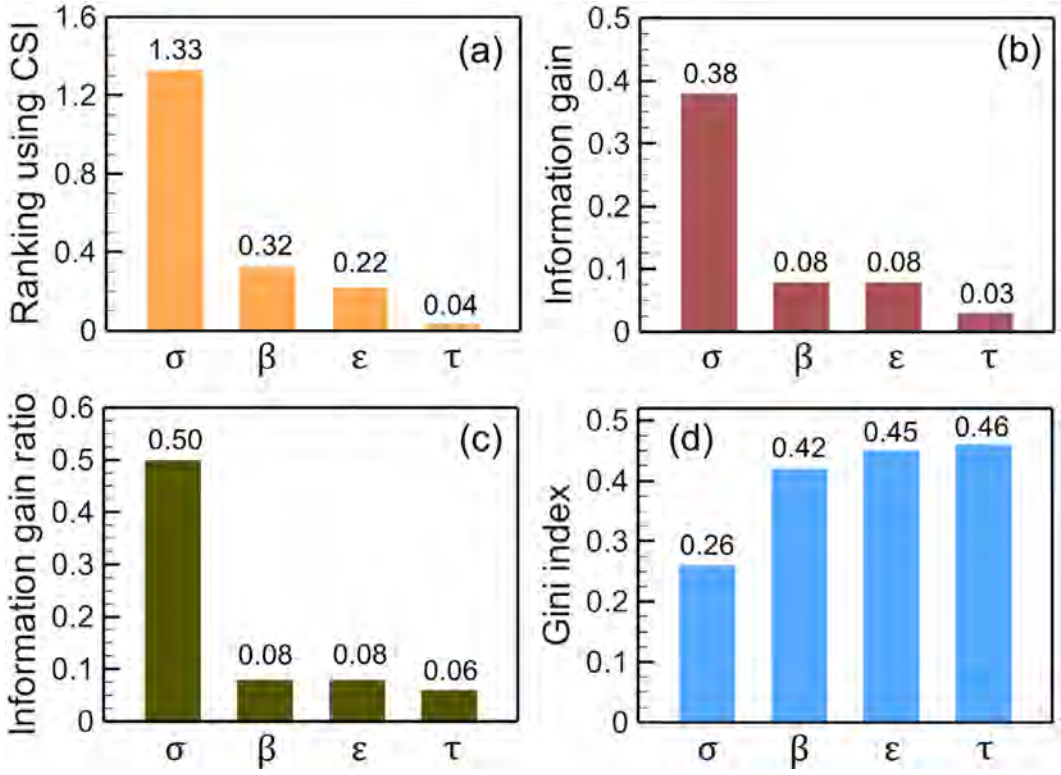


**Fig. 6. The comparative influence of four mechanistic variables on cracking.** The comparative influence is predicted using **(a)** the CSI from Eq. (2) **(b)** the information gain (IG) **(c)** the information gain ratio (IGR) and **(d)** the Gini index (GI). The variables $\sigma$, $\beta$, $\varepsilon$, and $\tau$ indicate the computed values of solidification stress (in MPa), the ratio of vulnerable and relaxation times, the temperature gradient to the solidification growth rate ratio (in K-s/mm$^2$), and cooling rate (in K/s) respectively.

The calculated values of CSI can be used to predict cracking susceptibility before printing. The values of CSI higher than 0.5 indicate the formation of cracks. An example, considering two sets of experimental data with and without cracks in PBF-L of 6061 Al is shown in Fig 5 [9]. The calculated values of CSI for those two experimental cases are shown in Fig. 5 which agrees with their respective experimental finding. Since the calculation of CSI is based on data collected from different sources, the difference due to machine-to-machine variations in part quality is implicitly accounted for in this approach.

### 3.3. Comparative influence of variables and cracking susceptibility maps

The comparative influence of the four mechanistic variables on crack formation is evaluated using their respective coefficients in Eq. (2). The midrange values of the four mechanistic variables are multiplied with their respective coefficients (Table 2) to evaluate their impacts. Solidification stress is found to be the most important factor affecting cracking followed by the ratio of the vulnerable and the relaxation times and the temperature gradient to the solidification growth rate ratio (Fig. 6a). The cooling rate has the least influence on cracking (Fig. 6a). The three classification indices of ML, IG (Fig. 6b), IGR (Fig. 6c), and GI (Fig. 6d) also show the same comparative influence as above. The calculations of the three indices are described in the supplementary document. Solidification stress has the highest values of both IG and IGR indicating its role as the most influential variable affecting cracking. It also has the lowest value of GI which further ascertains its most important contribution towards the crack formation. The comparative influence of variables on cracking will help to select appropriate values of variables to avoid crack formation.

Five cases each for crack (Fig 7a) and crack-free (Fig 7b) conditions were randomly selected from the 102 data and paired with their four computed mechanistic variables and the crack susceptibility index. The bar graphs in Fig. 7(a) represent the contribution of the individual mechanistic variables to the values of CSI. In all five cases, the prominent influence of solidification stress is apparent from its large contribution. The contribution of solidification stress was so large that the control of solidification morphology in many cases will not guarantee crack-free deposition. In all cases, the ratio of vulnerable times to relaxation times was the second most contributing factor in the crack formation. In contrast, the contribution of the cooling rate is negligible in all five cases. The solid line in this plot represents the values of CSI for the five cases computed using Eq. (2). In all five cases, the CSI values higher than 0.5 indicate the high susceptibility to crack formation. Fig. 7b shows the results of five specimens that showed the absence of cracks. Again the main contributor for the high susceptibility was the solidification stress. The cooling rate shows a beneficial contribution by reducing cracks due to its negative coefficient in Eq. (2). However, when the contributions of each mechanistic variable were added together, the computed CSI values were each lower than 0.5 indicating a high propensity of avoiding cracks as shown by the solid line. The figures show that although the contributions by the individual mechanistic variables vary in different cases, it is the combined effect that determines the susceptibility of crack formation and consideration of an individual factor, no matter how important, cannot provide a complete view of the susceptibility to crack formation.

The calculated CSI for various processing conditions is used to generate cracking susceptibility maps which show process windows to avoid cracks (Fig. 8a and 8b). The CSI in these maps shows a trend that is observed in the existing methodology to control cracking. For example, prevention of cracking (low CSI) by increasing the preheat temperature is a well-recognized technique used

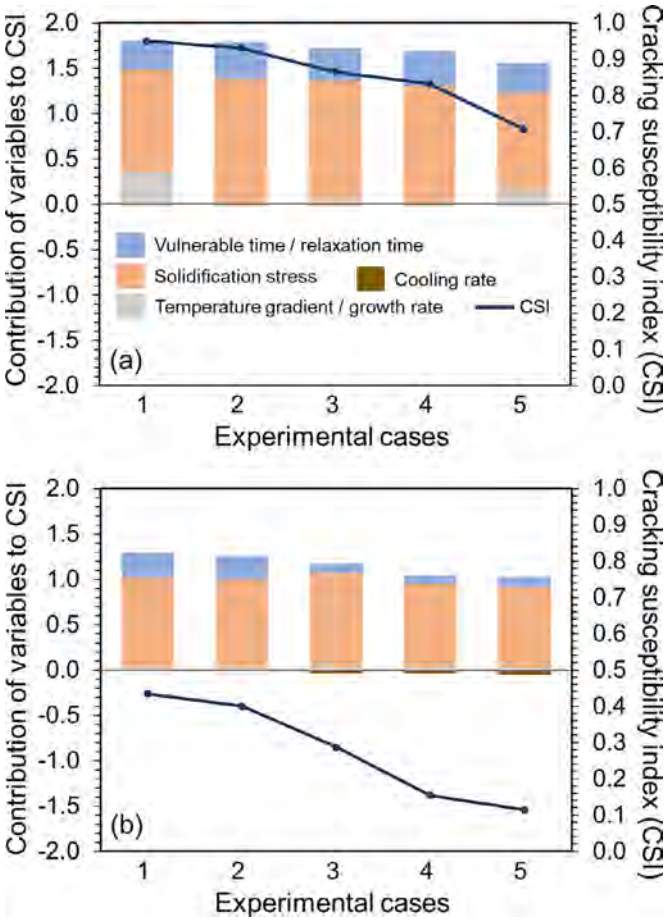


**Fig. 7. The contribution of the four mechanistic variables on cracking susceptibility index (CSI).** The individual contributions of the four mechanistic variables on CSI along with the CSI values are shown for five experiments from the literature with both the **(a)** presence and **(b)** absence of cracks. The CSI increases with the increasing ratio of the temperature gradient to growth rate, solidification stress, and the ratio of vulnerable and relaxation times because of their positive coefficients in Eq. (2). The cooling rate shows a beneficial contribution due to their negative coefficients in Eq. (2). Cracks were observed at CSI higher than 0.5 while values less than 0.5 had no cracks.

in both fusion welding as well as in additive manufacturing. In addition, we consider several experimental data with and without cracks for PBF-L of 6061 Al from the literature [24,26] to evaluate the applicability of the maps. The CSI values for these experiments indicated in both Fig. 8a and 8b agrees with their respective experimental evidence.

The preheat temperature, speed, and power affect the different mechanistic variables differently. These mechanistic variables can change widely depending on the process variables. The CSI maps (Fig 8a and 8b) can provide a practical approach to address the cracking issue. High powers and high preheat temperatures are used to control cracking [9, 46]. Changes in layer thickness and hatch spacing do not significantly affect the CSI because they do not change the mechanistic variables considerably. For example, the cooling rate changes by 2.6% for a change in layer thickness from 25 $\mu$m to 35 $\mu$m when other parameters are kept constant [47]. Similarly, the cooling rate changes only 2.8% for a change in hatch spacing from 35 $\mu$m to 110 $\mu$m [47]. Therefore, in the range of layer thickness and hatch spacing that are typically used in PBF-L, significant changes in the four mechanistic variables and CSI will not occur. The ML approach in this work applies to the aluminum alloys and the range of process conditions indicated. A similar ML

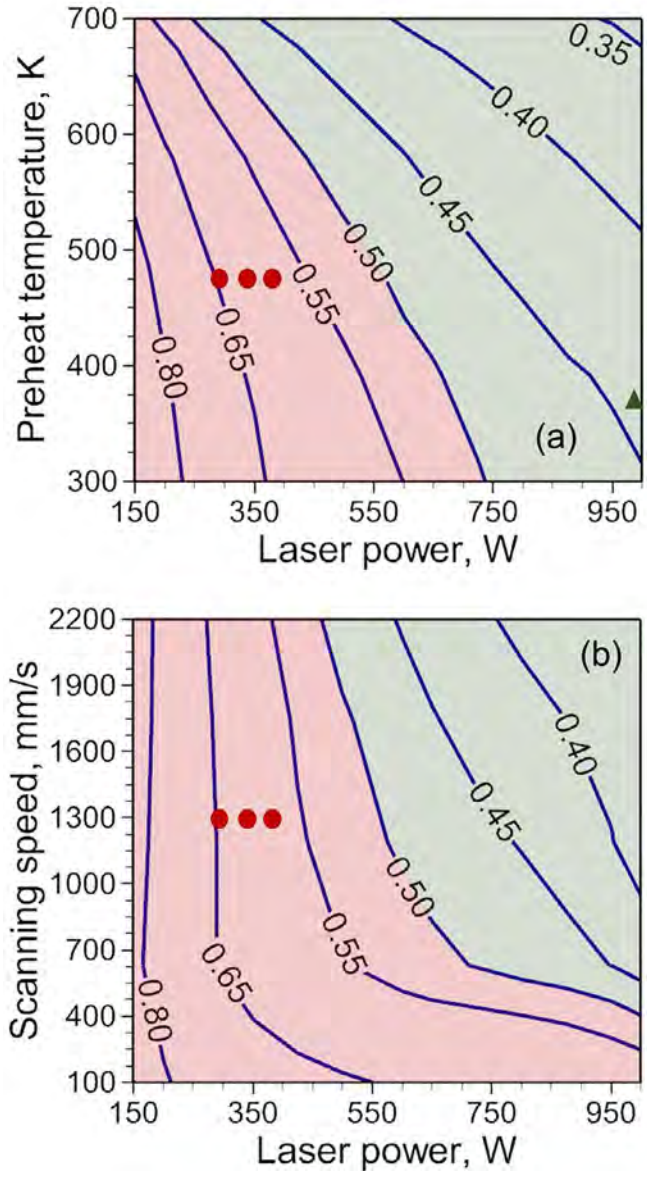


**Fig. 8. Cracking susceptibility maps.** The maps show the variation of CSI during PBF-L of 6061 Al with **(a)** laser power and preheat temperature at a fixed scanning speed of 1300 mm/s and **(b)** laser power and scanning speed at fixed preheat temperature of 473 K. The beam radius was 50 $\mu$m and the layer thickness was 30 $\mu$m. The values in the contour represent the CSI values. The red shaded region (with CSI greater than 0.5) indicates a zone of crack formation while the green shaded region (CSI less than 0.5) indicates crack free zone. The red dots [24] and green triangles [26] are data points taken from literature for validation.

approach is needed using mechanistic variables and data for other alloys to reveal insights into the cracking of the printed parts.

## 4. Summary and conclusions

Here we present a physics-informed machine learning analysis of cracking that considers different mechanisms of cracking of various alloys under different printing conditions. The computed mechanistic variables are then combined with the crack occurrence data to find a cracking susceptibility index and the comparative influence of the most important mechanistic variables on cracking.

We find that a user-friendly, verifiable cracking susceptibility index can predict the cracking of printed aluminum alloy parts accurately using the four mechanistic variables that embody the effects of both process variables and alloy properties. The four mechanistic variables, cooling rate, the temperature gradient to solidification growth rate ratio, solidification stress, and the ratio of vulnerable and relaxation times show their relations to crack formation using scientific principles. The solidification stress and cooling rate during solidification have the most and least influence on cracking, respectively for the PBF-L process variables and alloys studied. The comparative influence of the four variables to cracking as determined using the coefficient of the cracking susceptibility index matches with that found independently using information gain, gain ratio, and Gini index. We provide several cracking susceptibility maps where the CSI trends with the process variables are in agreement with the usual industrial practice of additive manufacturing and fusion welding.

## 5. Outlook

The methodology developed and tested in this paper and the findings point toward the following three unmistakable trends. First, the reduction of cracking using scientific principles will help to enhance quality, lower the cost of printed parts, and allow additive manufacturing of new alloys.

Second, since the mechanistic variables embody the effects of the process variables and alloy properties, the suitability of various alloys for a manufacturing process such as printability, weldability or castability can be explored using the approach developed and tested here. For example, the occurrence of porosity and surface roughness in additively manufactured parts can be addressed using a similar approach which will reduce defects, expedite qualification of parts, and enable printing of several alloys .

Third, the applicability of physics-informed machine learning to solve important problems is not limited to only additive manufacturing. The trend of variables needed to lower the occurrence of cracking is consistent with the industrial experience in fusion welding and casting. Thus, the approach will benefit other important manufacturing processes.

## Declaration of Competing Interest

The authors declare that they have no known competing financial interests or personal relationships that could have appeared to influence the work reported in this paper.

## Acknowledgments

Computations for this research were performed on the Pennsylvania State University's Institute for Computational and Data Sciences' Roar supercomputer. Funding for this research was provided by the 2020 industryXchange Multi-disciplinary Research Grants of the Pennsylvania State University .

## Supplementary materials

Supplementary material associated with this article can be found, in the online version, at doi:10.1016/j.actamat.2021.117612.

## Appendix

### *A1. Pearson's correlation for evaluating mutual independence of variables*

Variables used in ML may be mutually dependent on each other. Most ML algorithms cannot distinguish between these highly correlated variables. Therefore, dimensionality reduction by removing highly correlated variables is needed in the data preprocessing

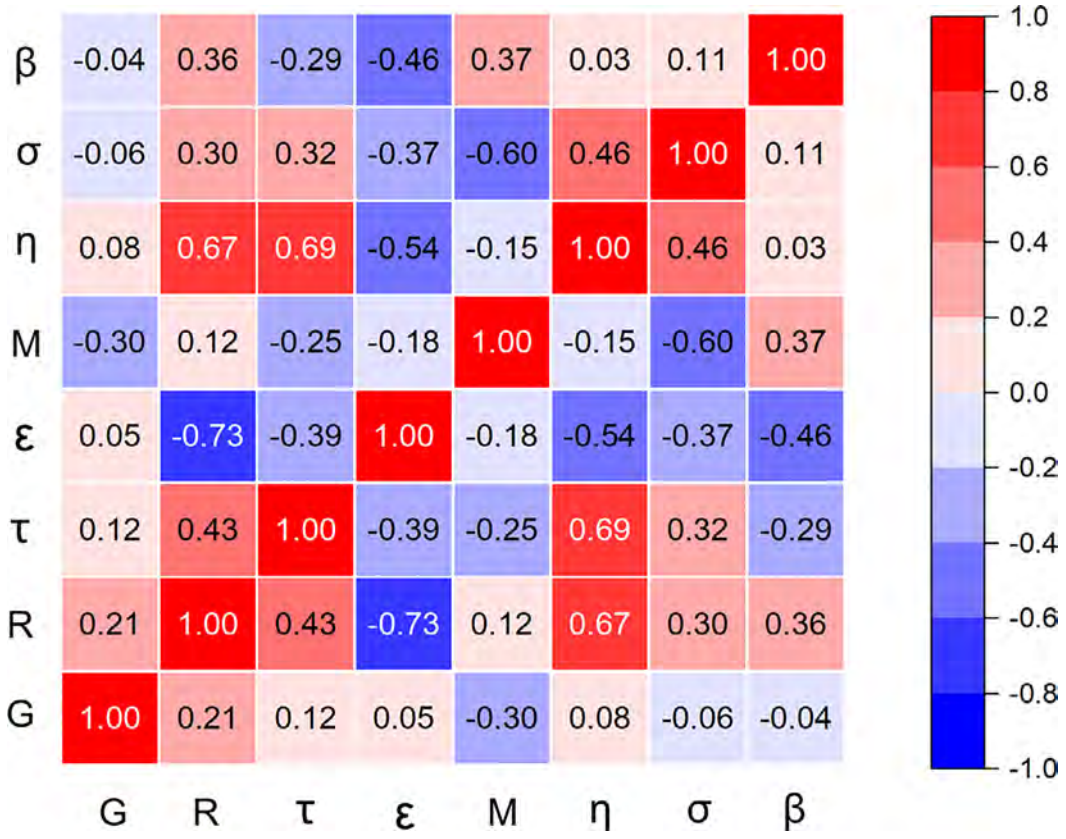


**Fig. A1.** Correlation between variables using Pearson's correlation.

step. Sets of highly correlated variables were identified using Pearson's correlation on the estimated values of the mechanistic variables.

$$\rho(x1, x2) = \frac{COV(x1, x2)}{\sigma_{x1}\sigma_{x2}} \tag{A1}$$

where $\rho$ is Pearson's coefficient, x1 and x2 are two variables, COV is the covariance function, and $\sigma$ represents the standard deviation of the variables. The mechanistic variables that may affect solidification cracking are temperature gradient (G), solidification growth rate (R), cooling rate ($\tau$) which is G times R, solidification morphology ($\varepsilon$) which is the ratio of G and R, mushy zone volume (M), aspect ratio of the molten pool represented by pool length to width ratio ($\eta$), the ratio of vulnerable to relaxation time ($\beta$) and solidification stress ($\sigma$). Pearson's correlation analysis can help us find the variables that can be used in machine learning without having the problem of mutual dependence. Pearson's coefficient varies between $-1$ and 1 wherein $-1$ indicates a strong negative correlation and 1 indicates a strong positive correlation (Fig. A1). Among highly correlated variables, only one is used for further analysis using ML. Pearson's correlation of greater than 0.5 has been used as a safe limit to determine whether variables are strongly correlate or not [44,45]. For example, the variable solidification stress ($\sigma$) has a high negative correlation with mushy zone volume (M). Since solidification cracking needs at least one mechanical criterion, the variable M is dropped, and $\sigma$ is retained. Similarly, pool aspect ratio ($\eta$) has a high correlation to all solidification parameters like cooling rate ($\tau$), solidification morphology ($\varepsilon$), and solidification growth rate (R). However, these solidification variables are fundamentally more important to cracking than the dimensional parameter of ($\eta$). Similarly, between $\varepsilon$ and R, $\varepsilon$ is retained as it controls the solidification morphology, and it also contains R. This exercise results in a total of 4 mechanistic variables, solidification stress ($\sigma$), the ratio of vulnerable time to relaxation time ($\beta$), solidification morphology ($\varepsilon$) and cooling rate ($\tau$) which are used in the ML analysis.

### *A2. Heat transfer and fluid flow model*

A transient, 3D heat transfer and fluid flow model [21] of powder bed fusion process was used to compute the mechanistic variables that affect cracking. The model considers the process parameters and thermophysical properties of alloys as inputs and provides temperature and velocity distributions in three dimensions from which the four mechanistic variables were computed. The properties of the three aluminum alloys utilized in the model are given in Table 1. The model and its implementation in PBF-L were described in our earlier publication [21,47]. The computational domain contains the powder bed, deposited layers, substrate, and shielding gas. An in-house Fortran code was developed for modeling which was compiled using an Intel Fortran Compiler. The model was run 102 times to compute the mechanistic variables corresponding to all 102 experimental cases. The following assumptions were made.

(a) The density of solid, powder, and liquid and the viscosity of liquid are assumed to be independent of temperature.
(b) The deposited layers and hatches are assumed to have flat surfaces.
(c) The liquid metal is assumed to be Newtonian and incompressible.
(d) The loss of alloying elements due to vaporization and the resulting composition change is not considered.

### A3. Scheil curve

The Scheil curve represents the relation between the temperature and solid fraction during the solidification of an alloy. Fig. A2 shows the Schiel curves for different aluminum alloys considered in this work. The Scheil curves were simulated using a commercial software ThermoCalc.

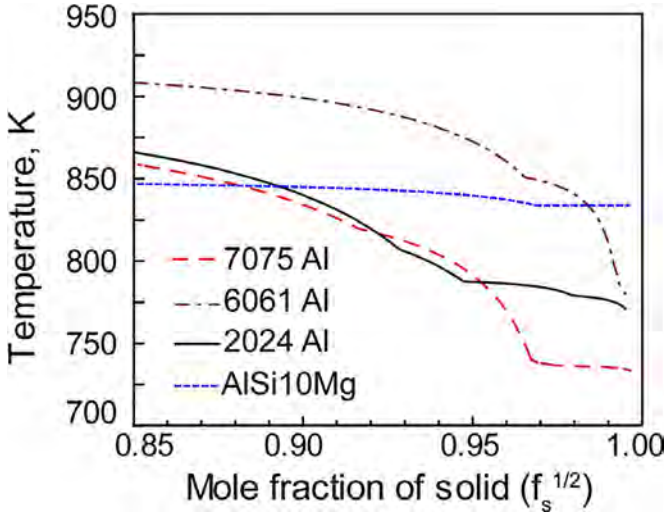


**Fig. A2.** The variation of square root of fraction solid ($f_s$) with temperature during solidification of different aluminum alloys. The maximum slope ($|dT/d(f_s)^{1/2}|$) of temperature versus $(f_s)^{1/2}$ curves is related to the susceptibility to crack formation.

## References


[1] T. DebRoy, T. Mukherjee, H.L. Wei, J.W. Elmer, J.O. Milewski, Metallurgy, mechanistic models and machine learning in metal printing, Nat. Rev. Mater. 6 (2021) 48–68.
[2] T. DebRoy, T. Mukherjee, J.O. Milewski, J.W. Elmer, B. Ribic, J.J. Blecher, W. Zhang, Scientific, technological and economic issues in metal printing and their solutions, Nat. Mater. 18 (2019) 1026–1032.
[3] T. DebRoy, H.L. Wei, J.S. Zuback, T. Mukherjee, J.W. Elmer, J.O. Milewski, A.M. Beese, A. Wilson-Heid, A. De, W. Zhang, Additive manufacturing of metallic components – process, structure and properties, Prog. Mater. Sci. 92 (2018) 112–224.
[4] H.L. Wei, T. Mukherjee, W. Zhang, J.S. Zuback, G.L. Knapp, A. De, T. DebRoy, Mechanistic models for additive manufacturing of metallic components, Prog. Mater. Sci. 116 (2021) 100703.
[5] T. DebRoy, H.K.D.H. Bhadeshia, Innovations in Everyday Engineering Materials, 1st ed., Springer, Switzerland, 2021.
[6] Y. Li, H. Li, L. Katgerman, Q. Du, J. Zhang, L. Zhuang, Recent advances in hot tearing during casting of aluminium alloys, Prog. Mater. Sci. 117 (2021) 100741.
[7] C.J. Todaro, M.A. Easton, D. Qiu, D. Zhang, M.J. Bermingham, E.W. Lui, M. Brandt, D.H. StJohn, M. Qian, Grain structure control during metal 3D printing by high-intensity ultrasound, Nat. Commun. 11 (2020) 142.
[8] J.H. Martin, B.D. Yahata, J.M. Hundley, J.A. Mayer, T.A. Schaedler, T.M. Pollock, 3D printing of high-strength aluminium alloys, Nature 549 (2017) 365–369.
[9] S.Z. Uddin, L. E.Murr, C.A. Terrazas, P. Morton, D.A. Roberson, R.B. Wicker, Processing and characterization of crack-free aluminum 6061 using high-temperature heating in laser powder bed fusion additive manufacturing, Add. Manufac. 22 (2018) 405–415.
[10] H. Zhang, H. Zhu, T. Qi, Z. Hu, X. Zeng, Selective laser melting of high strength Al–Cu–Mg alloys: processing, microstructure and mechanical properties, Mater. Sci. Eng. A 656 (2016) 47–54.
[11] A. Aversa, G. Marchese, A. Saboori, E. Bassini, D. Manfredi, S. Biamino, D. Ugues, P. Fino, M. Lombardi, New aluminum alloys specifically designed for laser powder bed fusion: a review, Materials. 12 (2019) 1007.
[12] T. Boellinghaus, J.C. Lippold, C.E. Cross, Cracking Phenomena in Welds IV, Springer International Publishing, Switzerland, 2016.
[13] T. Soysal, S. Kou, A simple test for assessing solidification cracking susceptibility and checking validity of susceptibility prediction, Acta Mater 143 (2018) 181–197.
[14] J. Liu, S. Kou, Susceptibility of ternary aluminum alloys to cracking during solidification, Acta Mater 125 (2017) 513–523.
[15] N. Coniglio, C.E. Cross, Effect of weld travel speed on solidification cracking behavior. Part 1: weld metal characteristics, Int. J Adv. Manufact. Technol. 107 (2020) 5011–5023.
[16] J.A. Williams, A.R.E. Singer, Deformation, strength, and fracture above the solidus temperature, J. Inst. Metal. 96 (1968) 5–11.
[17] M. Raissi, A. Yazdani, G.E. Karniadakis, Hidden fluid mechanics: learning velocity and pressure fields from flow visualizations, Science 367 (2020) 1026–1030.
[18] S. Karimpoulia, P. Tahmasebi, Physics informed machine learning: seismic wave equation, Geosci. Front. 11 (2020) 1993–2001.
[19] Y. LeCun, Y. Bengio, G. Hinton, Deep learning, Nature 521 (2015) 436–444.
[20] I.M. Jordan, T.M. Mitchell, Machine learning: trends, perspectives, and prospects, Science 349 (2015) 255–260.
[21] T. Mukherjee, H.L. Wei, A. De, T. DebRoy, Heat and fluid flow in additive manufacturing—Part I: modeling of powder bed fusion, Comput. Mater. Sci. 150 (2018) 304–313.
[22] C.E. Roberts, D. Bourell, T. Watt, J. Cohen, A novel processing approach for additive manufacturing of commercial aluminum alloys, Phys. Proced. 83 (2016) 909–917.
[23] E. Brandl, U. Heckenberger, V. Holzinger, D. Buchbinder, Additive manufactured AlSi10Mg samples using selective laser melting (SLM): microstructure, high cycle fatigue, and fracture behavior, Mater. Des. 34 (2012) 159–169.
[24] A.H. Maamoun, Y.F. Xue, M.A. Elbestawi, S.C. Veldhuis, Effect of selective laser melting process parameters on the quality of Al alloy parts: powder characterization, density, surface roughness, and dimensional accuracy, Materials (Basel) 11 (2018) 2343.
[25] D. Buchbinder, H. Schleifenbaum, S. Heidrich, W. Meiners, J. Bültmann, High power selective laser melting (HP SLM) of aluminum parts, Phys. Proced. 12 (2011) 271–278.
[26] L.E. Loh, Z.H. Liu, D.Q. Zhang, M. Mapar, S.L. Sing, C.K. Chua, W.Y. Yeong, Selective Laser Melting of aluminium alloy using a uniform beam profile, Virtual Phys Prototyp 9 (2014) 11–16.
[27] G. Agarwal, A. Kumar, I.M. Richardson, M.J.M. Hermans, Evaluation of solidification cracking susceptibility during laser welding in advanced high strength automotive steels, Mater. Des. 183 (2019) 108104.
[28] T. Soysal, S. Kou, Role of liquid backfilling in reducing solidification cracking in aluminium welds, Sci. Technol. Weld. Join. 25 (2020) 415–421.
[29] G. Agarwal, M. Amirthalingam, S.C. Moon, R.J. Dippenaar, I.M. Richardson, M.J.M. Hermans, Experimental evidence of liquid feeding during solidification of a steel, Scripta Mater 146 (2018) 105–109.
[30] J. Antony, Design of Experiments for Engineers and Scientists, 2nd Ed., Elsevier, Netherlands, 2014.
[31] N. Coniglio, C.E. Cross, Initiation and growth mechanisms for weld solidification cracking, Int. Mater. Rev. 58 (2013) 375–397.
[32] M.A. Easton, D.H. StJohn, Improved prediction of the grain size of aluminum alloys that includes the effect of cooling rate, Mater. Sci. Eng. A. 486 (2008) 8–13.
[33] H.L. Wei, J.W. Elmer, T. DebRoy, Three-dimensional modeling of grain structure evolution during welding of an aluminum alloy, Acta Mater 126 (2017) 413–425.
[34] S. Kou, Welding Metallurgy, 3rd ed., John Wiley & Sons Inc., New Jersey, 2020.
[35] S. Geng, P. Jiang, X. Shao, G. Mi, H. Wu, Y. Ai, C. Wang, C. Han, R. Chen, W. Liu, Y. Zhang, Effects of back-diffusion on solidification cracking susceptibility of Al-Mg alloys during welding: a phase-field study, Acta Mater 160 (2018) 85–96.
[36] N. Coniglio, C.E. Cross, Effect of weld travel speed on solidification cracking behavior. Part 3: modeling, Int. J. Adv. Manufact. Technol. 107 (2020) 5039–5051.
[37] T.W. Clyne, M. Wolf, W. Kurz, The effect of melt composition on solidification cracking of steel, with particular reference to continuous casting, Metal. Trans. B 13 (1982) 259–266.
[38] L. Aucott, D. Huang, H.B. Dong, S.W. Wen, J.A. Marsden, A. Rack, A. C. F. Cocks, Initiation and growth kinetics of solidification cracking during welding of steel, Sci. Rep. 7 (2017) 1–10.
[39] J. Liu, P. Zeng, Y. Wu, S. Kou, Determination of tensile strain causing solidification cracking in welding, Sci. Technol. Weld. Join. 25 (2020) 431–437.
[40] WEKA 3.8.5, University of Waikato, New Zealand, 1999-2020 available athttps://www.cs.waikato.ac.nz/ml/weka/ accessed on 08/15/2020.
[41] C. Barr, S.D.Sun Sun, M. Easton, N. Orchowski, N. Matthews, M. Brandt, Influence of macrosegregation on solidification cracking in laser clad ultra-high strength steels, Surf. Coat. Technol. 340 (2018) 126–136.
[42] G. Liu, D. Du, K. Wang, Z. Pu, B. Chang, Hot cracking behavior and mechanism of the IC10 directionally solidified superalloy during laser re-melting, Vacuum 181 (2020) 109563.
[43] M. Opprecht, J.P. Garandet, G. Roux, C. Flament, M. Soulier, A solution to the hot cracking problem for aluminium alloys manufactured by laser beam melting, Acta Mater 197 (2020) 40–53.
[44] D. Dai, T. Xu, X. Wei, G. Ding, Y. Xu, J. Zhang, H. Zhang, Using machine learning and feature engineering to characterize limited material datasets of high-entropy alloys, Comput. Mater. Sci. 175 (2020) 09618.
[45] C. Wen, Y. Zhang, C. Wang, D. Xue, Y. Bai, S. Antonov, L. Dai, T. Lookman, Y. Su, Machine learning assisted design of high entropy alloys with desired property, Acta Mater 170 (2019) 109–117.
[46] H. Hyer, L. Zhou, A. Mehta, S. Park, T. Huynh, S. Song, Y. Bai, K. Cho, B. McWilliams, Y. Sohn, Composition-dependent solidification cracking of aluminum-silicon alloys during laser powder bed fusion, Acta Mater 208 (2021) 116698.
[47] T. Mukherjee, H.L. Wei, A. De, T. DebRoy, Heat and fluid flow in additive manufacturing—Part II: powder bed fusion of stainless steel, and titanium, nickel and aluminum base alloys, Comput. Mater. Sci. 150 (2018) 369–380.